



Filament Eruption with a Deflection of Nearly 90 Degrees

Jiayan Yang¹ , Jun Dai^{1,2}, Hechao Chen^{1,2}, Haidong Li¹, and Yunchun Jiang¹

¹ Yunnan Observatories, Chinese Academy of Sciences, P.O. Box 110, Kunming 650011, People's Republic of China; yjy@ynao.ac.cn

² University of Chinese Academy of Sciences, Beijing 100049, People's Republic of China

Received 2018 January 11; revised 2018 May 31; accepted 2018 June 13; published 2018 July 25

Abstract

Using the data from the *Solar Dynamics Observatory*, the *Ahead of Solar Terrestrial Relations Observatory*, the Global Oscillation Network Group (GONG), and the Large Angle and Spectrometric Coronagraphs, the nearly 90° deflected eruption of a filament and the following coronal mass ejection (CME) occurring on the northern edge of AR 11123 on 2010 November 15 were presented in this paper. The filament was very small with the projected length of about 2.6×10^4 km and centered at about S23° W 38°. The potential-field source-surface model identified that the filament was located near the northern flank of a helmet streamer. The filament initially erupted northward to the nearby open fields with speeds from 151 to 336 km s⁻¹, resulting in a B7.6 subflare and some signatures of interchange reconnection. This suggested that the erupting filament interacted with the open fields at first. Then, guided by the highly-inclined open fields, it deflected about 90° southward on the plane of the sky to the magnetic minimum in the streamer configuration. In addition, the CME with the width of 64° and the central position angle of 221° was also deflected obviously in the inner corona to attain its final direction. Because the eruption failed to penetrate the open fields, these results corroborate the idea that open magnetic flux can act as a magnetic wall while a streamer belt can act as a potential well for coronal eruptions in the Sun.

Key words: Sun: activity – Sun: coronal mass ejections (CMEs) – Sun: filaments, prominences – Sun: flares – Sun: magnetic fields

Supporting material: animations

1. Introduction

Accurately forecasting space weather strongly relies on the knowledge of coronal mass ejection's (CME's) propagation trajectory in the solar corona and interplanetary space. Although a tentative geo-efficiency can hardly be derived solely from remote sensing observations, these data play an important role in the research of CME's trajectory near the Sun. Previous observations showed that, rather than along a constant straight trajectory, a CME could be deflected away from the radial direction of its solar source region (MacQueen et al. 1986; Cremades & Bothmer 2004), and a kinked structure in the solar source region of a CME seemed to be reflected in its 3D white-light structure (Bothmer & Mrotzek 2017), thus posing a direct influence on the geomagnetic effectiveness of a CME (Rodriguez et al. 2009; Mays et al. 2015). The deflection of a CME may occur in both the latitude and longitude (Byrne et al. 2010; Davies et al. 2013; Zhou & Feng 2013) in the interplanetary space, and it is considered as the result of the interaction between a CME and the ambient solar wind (Wang et al. 2004, 2014) or another CME (Lugaz et al. 2012). Since the strength of heliospheric magnetic fields decreases with the increase of the heliocentric distance (Shen et al. 2011; Zuccarello et al. 2012; Kay et al. 2013), it has been suggested that CME deflection should predominantly occur in the corona close to the Sun within a few solar radii, where the restoring force of the magnetic field acting on the CME is strong.

Many observations revealed that, erupting magnetic structures in the low corona such as jets, erupting filaments, and CMEs, can be channeled and guided by neighboring large-scale background magnetic fields during their early life, thus being deflected to the minimum in magnetic stresses on global scales (Nisticò et al. 2015). Many magnetic obstacles are able to

impose actions on coronal eruptions and hence alter their initial trajectories. Some typical magnetic obstacles have been identified, including active regions (ARs; Sterling et al. 2011; Sun et al. 2012; Kliem et al. 2013), coronal holes (CHs; Lugaz et al. 2011; Mäkelä et al. 2013; Zheng et al. 2016), and helmet streamers (Bemporad et al. 2005; Moore & Sterling 2007; Yang et al. 2011) or pseudostreamers (Bi et al. 2013; Lynch & Edmondson 2013; Yang et al. 2015). Recently, Möstl et al. (2015) and Wang et al. (2015) demonstrated that the propagation trajectory of a very fast CME on 2014 January 7 was along a nonradial direction due to the strong channeling effect of nearby AR magnetic fields. CHs can also act as a magnetic wall (Gopalswamy et al. 2009) so that CMEs may not penetrate their open magnetic fields (Kilpua et al. 2009).

On the other hand, there are two categories of coronal streamers according to Wang et al. (2007), named as the helmet streamer and the pseudostreamer. A helmet streamer is bounded by open fields of opposite polarities, generally containing an overlying Y-type null point; while a pseudostreamer is bounded by open fields of like polarities, containing an X-type null point. No matter what kind of coronal streamer it is, the coronal magnetic field's strength reaches the minimum at the null point; therefore a streamer belt can act as a potential well to force CMEs to move toward it (Kay et al. 2013). Consequently, during solar minima, the polar CH magnetic fields tend to guide high latitude CMEs toward the equatorial streamer belts; whereas at other times of the solar cycle, the increased complexity of the coronal magnetic fields may lead to a wider variety in the deflection direction (Plunkett et al. 2001; Cremades et al. 2006; Xie et al. 2009; Bosman et al. 2012). Statistically, major flares often lie under the center of the associated CMEs that are consistent with the standard flare-CME model, while smaller flares show less symmetry and are widely spread to the edge of or even out of the CME span

(Yashiro et al. 2008). In line with previous results (Harrison 1986; Bemporad et al. 2005), Moore & Sterling (2007) concluded that there is a new subclass of CMEs, called “over-and-out CMEs,” coming from the explosion of a stressed, initially-closed magnetic field that simultaneously produces a flare in the outskirts of a streamer base. They also proposed a so-called magnetic-arch-blowout scenario to interpret the basic way of how this kind of CMEs is produced. In this scenario, a magnetic explosion produces a flare as well as a plasmoid guided by the streamer arcade in the inner corona, then it blows out the top of the streamer arcade, and becomes a CME propagating radially in the outer corona.

Filament eruptions also tend to deviate systematically in latitude from the centers of related CMEs (Simnett 2000). Therefore, nonradial filament eruptions are not uncommon (Bemporad 2009; Li et al. 2010; Joshi & Srivastava 2011; Shen et al. 2011; Yan et al. 2013). Consistent with the model of Filippov & Gopalswamy (2001), some observations showed that streamers and neighboring CHs could influence the behavior of filaments and hence guide their eruptions (Jiang et al. 2009; Panasenco et al. 2011; Yang et al. 2012a). Most deflections mentioned above were caused by the guidance of backgrounds, however, in some extreme situations, erupting filaments can interact with the background obstacles directly and show clear coronal imprints such as the destruction of streamers or the shrink of CHs. Jiang et al. (2007b) reported such an example. When a small filament obliquely erupted westward, it encountered a remote CH in the way. The filament eruption was blocked by the CH, and then its trajectory deflected eastward. The associated halo-type CME was bounced by the CH too, so it turned back together with the filament. In this sense, this eruption had already completed a longitudinal deflection of almost 180° near the solar surface. During this period of time, the CH was clearly disturbed. Weak brightenings appeared along the CH boundary and extended into its interior eventually, resulting in the shrink of the CH’s area and the change of the CH’s shape. In addition, Yang et al. (2015) gave an example to show credible observation signatures of interchange reconnection (Crooker et al. 2002) between open and closed magnetic fields carrying a filament. The interchange reconnection was driven by filament eruption inside a pseudostreamer bounded by two CHs. Guided by the nearby CH, the erupting field approached and then reconnected with the remote CH that had the open field with opposite polarity. As a result, obvious remote brightenings were produced along the boundary of the remote CH.

On 2010 November 15, a filament erupted near the northern outskirts of the base of a helmet streamer, accompanied by a subflare and followed by a CME. Located outside instead of inside the streamer arcade, however, the filament initially erupted toward the nearby open fields and then underwent a large deflection up to 90° . This event thus gives us an opportunity to detail the interaction between the erupting field and the nearby open fields, as well as the cause of the deflection.

2. Data and Instruments

The event on 2010 November 15 took place at the northern part of AR 11123 around 14:36 UT and was observed by multiple spacecraft and ground-based telescopes. Here we mainly used the high-spatial and temporal resolution observations from the Atmospheric Imaging Assembly (AIA; Lemen et al. 2012)

and the Helioseismic and Magnetic Imager (HMI; Scherrer et al. 2012) aboard the *Solar Dynamics Observatory* (*SDO*; Pesnell et al. 2012), combined with the Extreme Ultra-Violet Imager Telescope (EUVI; Wuelser et al. 2004) aboard the *Ahead of Solar Terrestrial Relations Observatory* (*STEREO-A*; Kaiser et al. 2008) spacecraft from a different view. AIA provides full-disk images at 9 UV and EUV wavelengths, with the pixel size of $0''.6$ and the time cadence up to 12 seconds. In the present study, the level 1.5 images of 4 EUV channels centered at 131 \AA (Fe XX, $\log T = 7.0$), 193 \AA (Fe XII, $\log T = 6.1$), 211 \AA (Fe XIV, $\log T = 6.3$), and 304 \AA (He II, $\log T = 4.7$) were used. HMI measures full-disk line-of-sight magnetic fields in the Fe I absorption line at 6173 \AA . Its spatial sampling is $0''.5\text{ pixel}^{-1}$, time cadence is 45 seconds, and the precision is 10 G. In this event, the full-disk EUV images from *STEREO-A/EUVI* at 3 passbands of 304, 171, and 195 \AA were also used. The field of view (FOV) of these images is about $1.5 R_\odot$, the pixel size is $1''.6$, and the time cadences ranged from 1 to 3 minutes. On 2010 November 15, *STEREO-A* was about 84° ahead of Earth. Therefore, the eruptive region was in the southwest of the solar disk in *SDO* images, but was close to the southeast limb when seen from *STEREO-A*. Full-disk $H\alpha$ observations from the Global Oscillation Network Group (GONG) at the National Solar Observatory (NSO) were presented, with the pixel size of $1''$ and the time cadence of 1 minute. All these data were processed using the standard software programs in SolarSoftWare (SSW), and then rotated differentially to a reference time near the eruption.

To explore the white-light corona structures involved in this event and identify the associated CME, we checked the C2 white-light coronagraph data from the Large Angle and Spectrometric Coronagraphs (LASCO; Brueckner et al. 1995) on board the *Solar and Heliospheric Observatory* (*SOHO*). The LASCO data cover the range of $2\text{--}6 R_\odot$. We also used observations from the COR1 and COR2 coronagraphs on board *STEREO-A* (Howard et al. 2008), with the FOVs of $1.4\text{--}4.0$ and $2.0\text{--}15.0 R_\odot$, respectively. Finally, the soft X-ray (SXR) light curves observed by the *Geostationary Operational Environmental Satellite* (*GOES*) were used to follow the flare time.

3. Observational Phenomena and Analysis

Accompanied by a *GOES* B7.6 X-ray flare and followed by a CME, a filament erupted from AR 11123 at around 14:36 UT on 2010 November 15. The X-ray flare started at 14:36 UT, reached the peak at 14:42 UT, and ended at 14:48 UT. The general situation of the region before the eruption is shown in Figure 1. The filament lies at the northern boundary of AR 11123 and its centroid was located at about $S23^\circ W38^\circ$. In the pre-eruptive AIA cool 304 (panel (d)) and hot 131 \AA (panel (e)) images, the filament showed up as a dark S-shaped feature. The projected length of the filament was only about 2.6×10^4 km, slightly longer than that of minifilaments with the average projected length of 1.9×10^4 km (Wang et al. 2000). As expected, the filament separated opposite-polarity fields and thus resided above the polarity inversion boundary between them, as seen from the outlines of the pre-eruptive 304 \AA axis of the filament superimposing on the corresponding HMI magnetogram (panels (c) and (f)). The thick arrows showed a larger negative-polarity quiet-Sun region northwest to the filament, where the filament would erupt toward later. As a reference direction to compare with that of the associated CME,

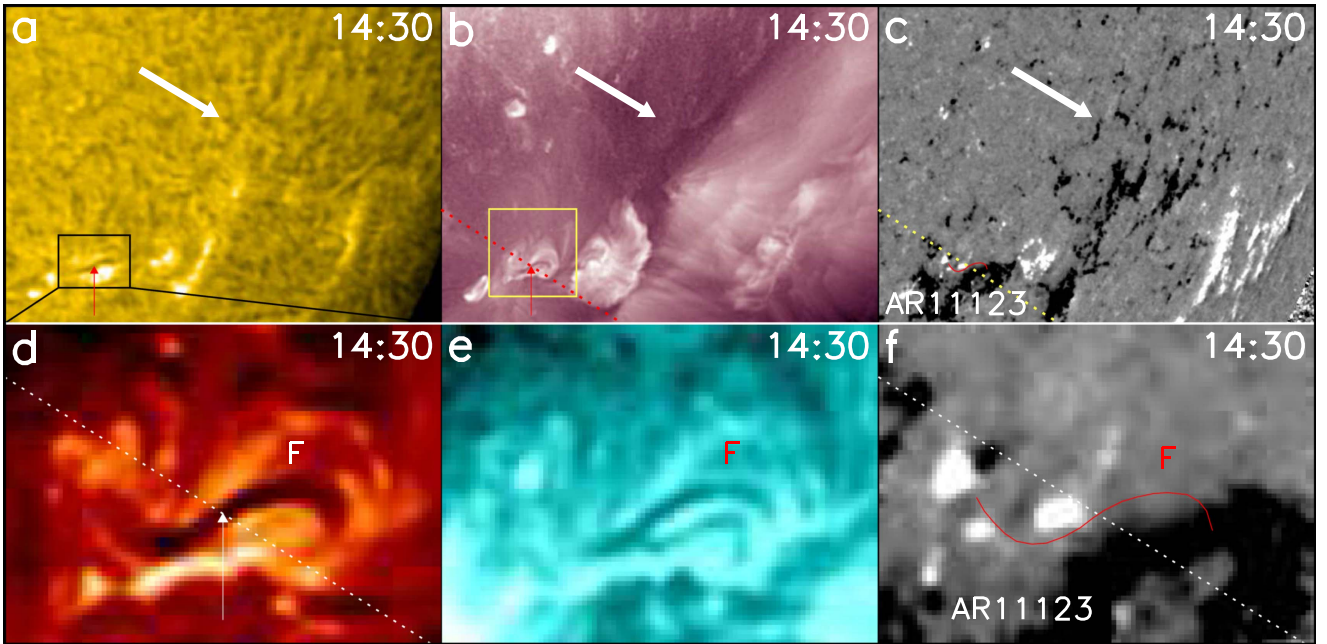


Figure 1. General appearance of the eruptive region before the eruption of a filament at 14:30 UT on 2010 November 15. Top row: GONG H α image (a), AIA 211 \AA image (b), and HMI magnetogram (c). Bottom row: the close-up view of the filament in AIA 304 \AA image (d), 131 \AA image (e), and HMI magnetogram (f). The thin arrows indicate the centroid of the filament, while the thick arrows indicate a negative-polarity quiet-Sun region. The field of view (FOV) is 330'' \times 240'' for the top row. As indicated by the black box, it is 54'' \times 40'' for the bottom row. The yellow box indicates the FOV of Figure 3.

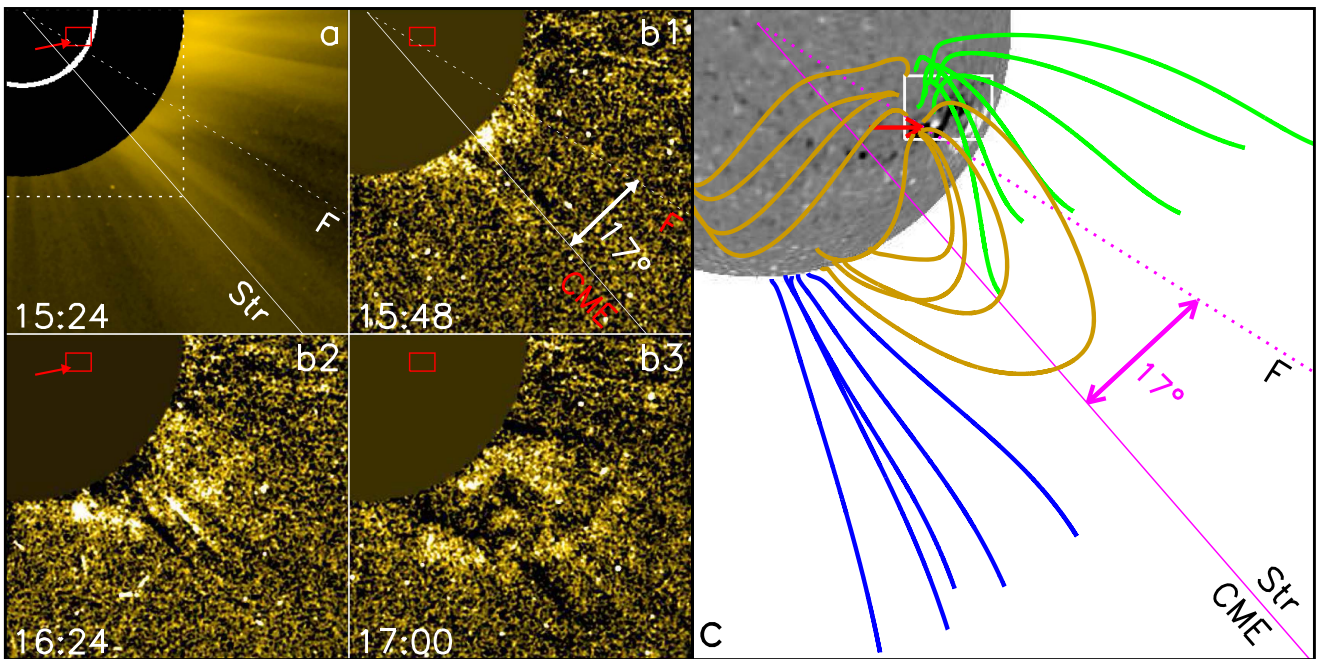


Figure 2. LASCO C2 white-light direct image (a) and running difference images (b1)–(b3) show the pre-existing coronal streamer Str and the CME evolution on 2010 November 15. The FOV is $4.71 R_\odot \times 4.46 R_\odot$. The dashed lines indicate the radial direction of the filament; the solid lines indicate the streamer's radial direction as well as the final CME direction. The solid boxes mark the eruptive region with the same FOV as that of the top row in Figure 1, while the dotted box marks the FOV of panel (c). (c) PFSS-extrapolated coronal field lines display the bipolar helmet-streamer configuration above the eruptive region on the same day.

The dotted lines in Figure 1 indicate the initial radial direction of the filament, which was a straight line connecting the centroid of the filament and the solar disk center. If a filament erupts perpendicular to the solar surface symmetrically, it will travel roughly along its radial direction (Loughhead et al. 1983; Yang et al. 2012b). Measured from the 14:30 UT AIA 304 \AA image, this direction was roughly 238° counterclockwise deviated from the north direction in the present event.

The pre-existing coronal structure and the CME evolution are shown in Figure 2. In this figure, the solid straight lines indicate the central position angle (PA) of the CME, which is roughly the projection of its propagation direction, while the dashed lines represent the projection of the filament's radial direction. At 15:48 UT, the LASCO C2 observation showed that the sequential CME first appeared above the southwest limb of the Sun. The width of the CME was 64° and the central

PA was 221° . The CME propagated nearly along the radial direction of a coronal streamer, which looked like a radial fan. It is noted that, however, the propagation direction of the CME was not consistent with the radial direction of the filament, but departed 17° southward from the filament on the plane of the sky. Using the potential-field source-surface (PFSS) software package, we obtained the large-scale magnetic topology below the streamer. The PFSS software package is based on the model of Schrijver & DeRosa (2003) and synoptic magnetic maps of HMI, available in SSW. The synoptic map used here was obtained at the time closest to the event, and the result is also presented in Figure 2 (panel (c)). Clearly, there is a PFSS-modeled bipolar structure below the streamer observed in LASCO C2, thus confirming that the streamer was a real helmet streamer rather than a pseudostreamer. It overlaid a single streamer arcade (shown by the brown curves) bounded by two open fields with opposite magnetic polarities (displayed by the blue and green curves). As indicated by the red arrow, the filament lies at the northern flank of the streamer arcade and the involving eruptive area indicated by the white box even intruded into the green open-field region.

The initial eruption of the filament is illustrated by the AIA observations as shown in Figure 3 (see the AIA animation of Figure 3 also). Around the time of the start of the flare, a bright patch close to the central part of the filament appeared (panel (a1)). Then the filament began to rise quickly and erupted bodily toward the northwestern direction. This process could be seen at multithermal EUV wavelengths of AIA (pointed out by the thick arrows in panels (a2), (a3), and (b)). Although the observations of AIA only provide us with the projected trajectory of the filament, it is clear that the filament moved along neither its original radial direction nor the central PA of the final CME. In fact, it deviated fairly far from them, with an intersecting angle of 80° and 97° , respectively, on the plane of the sky.

As mentioned before, this eruption was accompanied by a B7.6 X-ray flare. In addition to the flare, other three phenomena also appeared in this event: a remote bright ribbon, a small coronal dimming region, and a faint loop system. All of these four features are marked in Figure 3 and labeled as FL, RB, D, and L, respectively. The outlines of the pre-eruptive filament's axis at 304 \AA , the remote bright ribbon at 304 \AA (14:39 UT), and the dimming region at 211 \AA (14:44 UT) images are superimposed on the HMI magnetogram (panel (d)). Typically, the flare consisted of two ribbons, which were on the opposite-polarity sides of the filament and moved away from each other (panels (a3) and (a4)). And then, post-eruptive EUV loops arose and connected them gradually (panels (c), (e), and (f)). Predominantly located over the negative-polarity region north of the original filament, the remote bright ribbon was distinct well from the flare ribbon. The dimming region developed on the negative-polarity region adjacent to the western end of the filament. As a transient feature that could be discerned only in a few 193 , 211 , and 335 \AA images after the flare peak, a faint loop system appeared to connect the positive-polarity region close to the northern ribbon of the flare and the negative-polarity region near the remote brightenings. All of these features were representative interchange reconnection signatures, as reported by Yang et al. (2015).

The further eruption of the filament is displayed in Figure 4 (see the AIA animation of Figure 4). As we can see, the progressive eruption of the filament along the initial path

persisted at all of AIA EUV wavelengths until about 14:45 UT (see the white thick arrow in panels (a2), (b), and (c)), and then the filament became invisible and its trace was lost. About 25 minutes later, an eruption similar to filament eruption arose from the northwest of the flare at about 15:10 UT. As indicated by the yellow thick arrows (panels (a3) and (d2)), such an eruption was fainter but thicker and wider than the initial eruption of the filament. Because this eruption is closed to the initial eruption in time, and there was not any other filament appearing to the northwest of the filament as shown in Figure 1, it was deduced that this eruption was the continuation of the initial eruption. In other words, it was originated from the same filament and represented its second eruption stage. This deduction is confirmed by the observations of *STEREO-A* from different views that will be detailed below. Surprisingly, the erupting filament underwent obvious deflection. On the plane of the sky, the projected route of the filament made a sudden clockwise turn of about 90° relative to that of the initial eruption, and thus tended toward the central PA of the final CME. The real trajectory of the erupting filament might not turn around so sharply due to the projection effects, but undoubtedly the deflection happened and the filament approached to the final direction of the CME eventually. In this sense, we suppose that the eruption of the filament could be related to the CME.

To investigate the reason of such a large deflection of the eruption, the zoomed-in HMI magnetogram of the eruptive region before eruption is presented in Figure 4(e), superimposing with the coronal magnetic field lines obtained by the PFSS model as well as the profiles of the filament, the remote brightenings, and the dimming region. Apparently, the filament was located near the base of the brown closed-field lines but outside it. These close-field lines represent the northern flank of the streamer arcade. The initial eruption direction of the filament was parallel to the legs of the green open-field lines, and the remote brightenings partially coincided with their footpoints. Both of these phenomena strongly implied the occurrence of interchange reconnection between the magnetic field of the filament and the northern open fields (Sterling & Moore 2001; Crooker & Webb 2006; Zheng et al. 2017). As suggested by Yang et al. (2015), such an interchange reconnection could simultaneously produce the remote brightenings, the dimming region, and the loop system during the initial eruption. In particular, the direction of the deflecting eruption was approximately consistent with the curvature of the open-field lines, which pointed northward initially, but subsequently bent westward and southward by large angles at greater heights. Based on this consistency, we suppose that the guiding action of the open fields should be responsible for the deflection of the later eruption.

The two-stage eruption of the filament and the formation of the remote brightenings, the dimming region, and the loop system could be displayed more clearly and comprehensively by the time slices made from AIA EUV images along three slits, St, Se (Se1), and Sd (indicated by the long arrows in Figures 3 and 4). St passed through the remote brightenings, the loop system, the flare, and the dimming region (see Figure 3), hence its time slices could reflect the spacetime relationships of these characteristics. Se (Se1) passed through the original centroid of the filament and orientated to the initial eruption direction; Sd pointed to the deflected eruption direction (see Figure 4). Therefore, their time slices reflected the processes of the initial eruption and the later

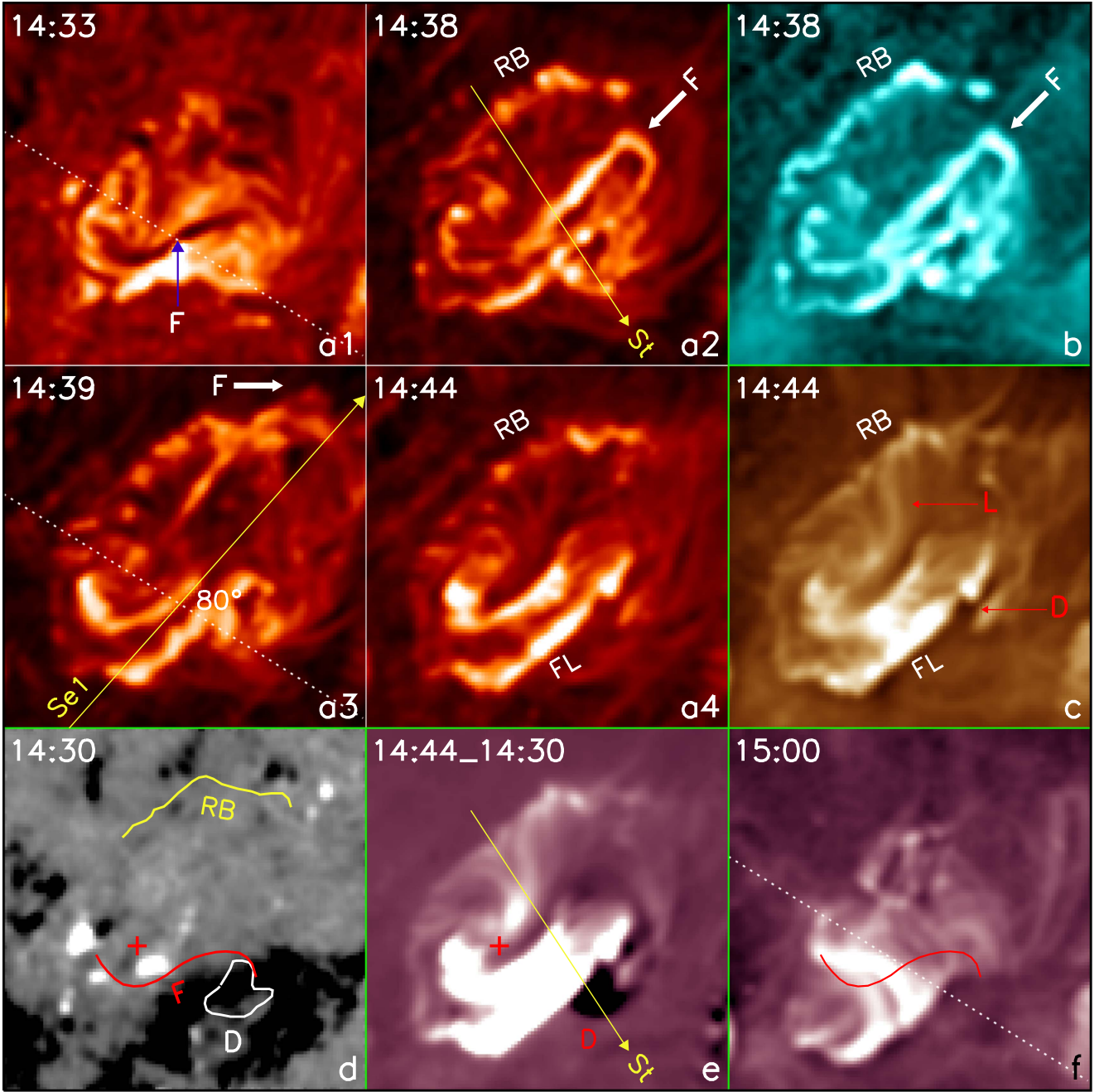


Figure 3. Close-up view of the initial filament eruption in the AIA 304 Å direct images (a1)–(a4), 131 Å direct image (b), 193 Å direct image (c), 211 Å direct image (f), and 211 Å fixed-base difference image (e). Panel (d) is the HMI magnetogram. The long arrows, St and Se1, indicate the slit positions of the time slices shown in Figure 5. The dashed lines show the radial direction of the filament. The filament, F, the flare, FL, the remote brightenings, RB, the coronal dimming region, D, and the loop system, L, are also indicated in the figure. The FOV is $66'' \times 66''$. (An animation corresponding to this figure is available, with the time from 14:20 UT to 15:20 UT on 2010 November 15 and the data from AIA 304, 193, 211, and 131 Å direct images.)

(An animation of this figure is available.)

deflection of the filament. The results are presented in Figure 5. It is noted that the initial eruption of the filament was nearly simultaneous with the occurrence of the remote brightenings and the start of the flare (panels (a1)–(a4)). The dimming region and the loop system began to appear immediately after the flare peak; and then the two ribbons of the flare separated gradually. The erupting filament became almost invisible after 14:45 UT. Panels (b1)–(b2) show that the erupting filament consisted of straight, bright multistreak structures. Applying linear fittings to the streaks indicates that their average speeds were from $151 \pm 12 \text{ km s}^{-1}$

to $336 \pm 19 \text{ km s}^{-1}$ on the plane of the sky. Afterwards, the deflected filament began to appear as a dark streak in 304 Å images after about 15:10 UT (panel (c)). The transformation of the apparent morphology of the erupting filament from the bright to dark streaks implies that it might undergo a plasma cooling during the time from 14:45 to 15:10 UT. The average projected speed of the filament in the later stage was about $22 \pm 1 \text{ km s}^{-1}$. This was much lower than the speed in the first stage, showing that the erupting filament was decelerated significantly in the same period of plasma cooling.

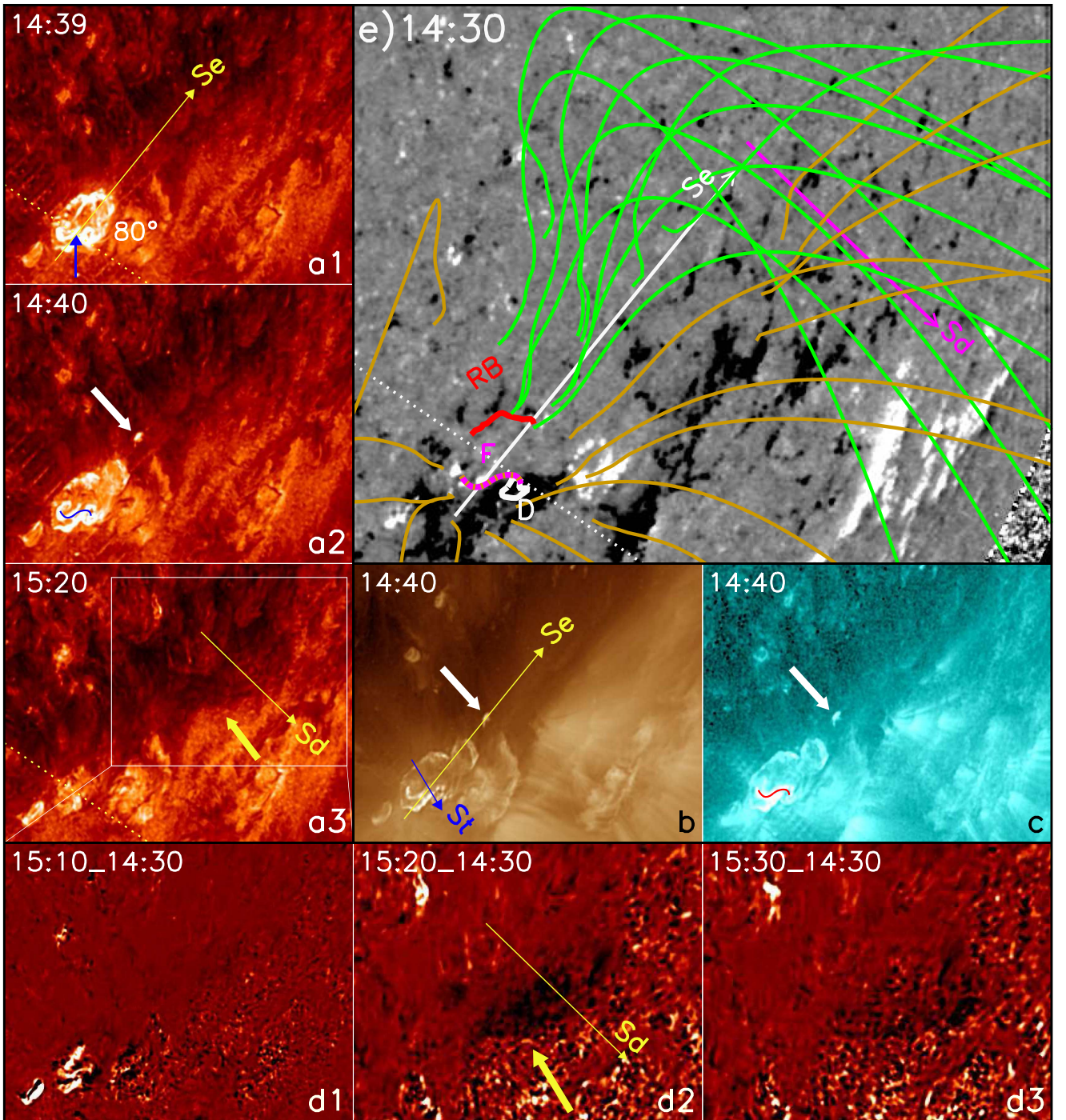


Figure 4. Further process of the filament eruption in AIA 304 Å (a1)–(a3), 193 Å (b), 131 Å (c) direct images, and 304 Å fixed-base difference images (d1)–(d3). The FOVs are $330'' \times 240''$ for the direct images and $223'' \times 162''$ for the fixed-base difference images. Panel (e) is the close-up view of the eruptive region in the HMI magnetogram, overlaid by the PFSS-extrapolated closed-field (brown) and open-field (green) lines. Se and Sd are the two slit positions of the time slices, and the other symbols have the same meaning as in Figure 3. (An animation corresponding to this figure is available, with the time from 14:00 UT to 16:00 UT on 2010 November 15 and the data from AIA 304 and 131 Å direct images.)

(An animation of this figure is available.)

All of the above phenomena and their consistent evolution can also be seen from the view of *STEREO-A* in Figure 6. The blue arrows indicate the original centroid of the filament F and the thick white arrows indicate the erupting filament. The red lines mark the filament's initial eruption direction, while the yellow lines mark its ultimate eruption direction. Clearly, the dark S-shaped filament could be discerned in EUVI-A 304 Å

images before the flare (panel (a1)). The eruption process could also be divided into two distinct stages. In the first stage, the filament erupted northeastward along a path indicated by the red lines (panels (c1), (b2), and (c3)). Then in the second stage, the erupting filament continuously rotated counterclockwise on the plane of the sky, and ultimately tended to a direction indicated by the yellow lines (panels (d1)–(d3)) with total

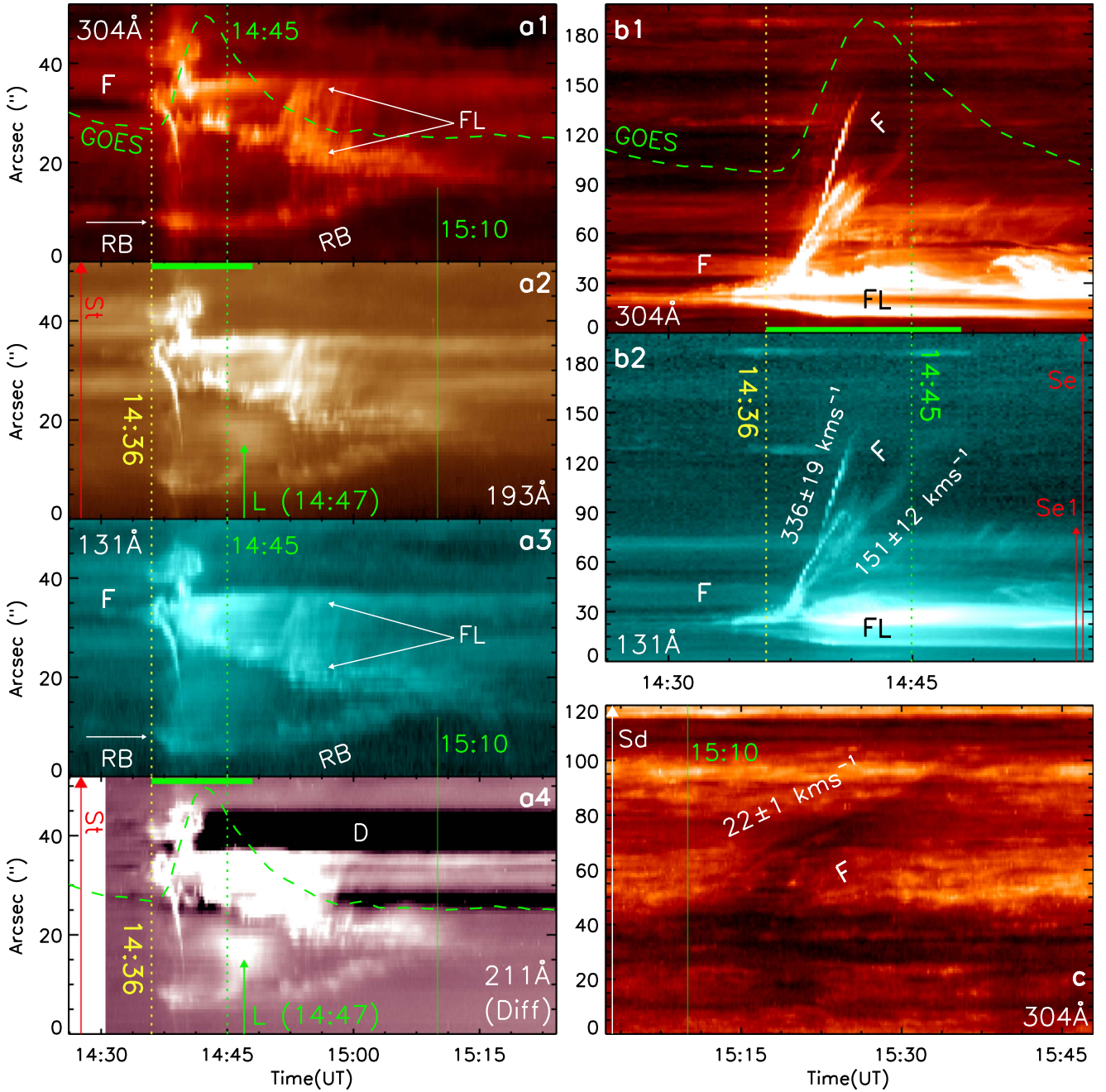


Figure 5. Time slices from AIA EUV images for the slits St(a1)–(a4), Se, and Se1(b1)–(b2), and Sd (c) depicted in Figures 3 and 4. The time profile of the GOES 1–8 Å SXR flux is overplotted in an arbitrary unit to fit the panels, and the flare duration is superimposed as thick horizontal bars. The yellow dashed lines indicate the flare start time at 14:36 UT and the green dashed/solid lines indicate the end/start times of the initial/later F eruptions at 14:45/15:10 UT. The velocities of the filament eruption in different stages are also indicated.

rotation angle of about 46° . Particularly, from the view of STEREO-A, the two stages of the filament eruption were observed as continuous processes without the loss of the erupting filament (panels (d1)–(d3)). It directly proves that the two seemingly irrelevant eruptions in SDO observations from 14:45 to 15:10 UT (see Figures 4 and 5) were of a single filament eruption with a large deflection indeed. The remote brightenings, RB, the flare, FL, the loop system, L, and the dimming region, D, could also be identified clearly in EUVI-A images. Moreover, the initial filament eruption was pointed to the northern open-field region and the remote brightenings were very close to the footpoints of the green open-field lines

(panel (e)). These observations further strengthen the suggestion that the open field should first participate in and then guide the filament eruption to produce the remote brightenings and the sequent deflection of the filament.

Similar to the observations of LASCO C2 (see Figure 2), in the corresponding STEREO-A coronal images, the CME also propagated along a pre-existing streamer. This is shown in Figure 7 by COR1- and COR2-A images. Although both LASCO and STEREO observations are projected images, it still can be reasonably deduced that the real direction of the CME must be very close to or even coincide with that of the streamer, since they shared the same route when seen from two different

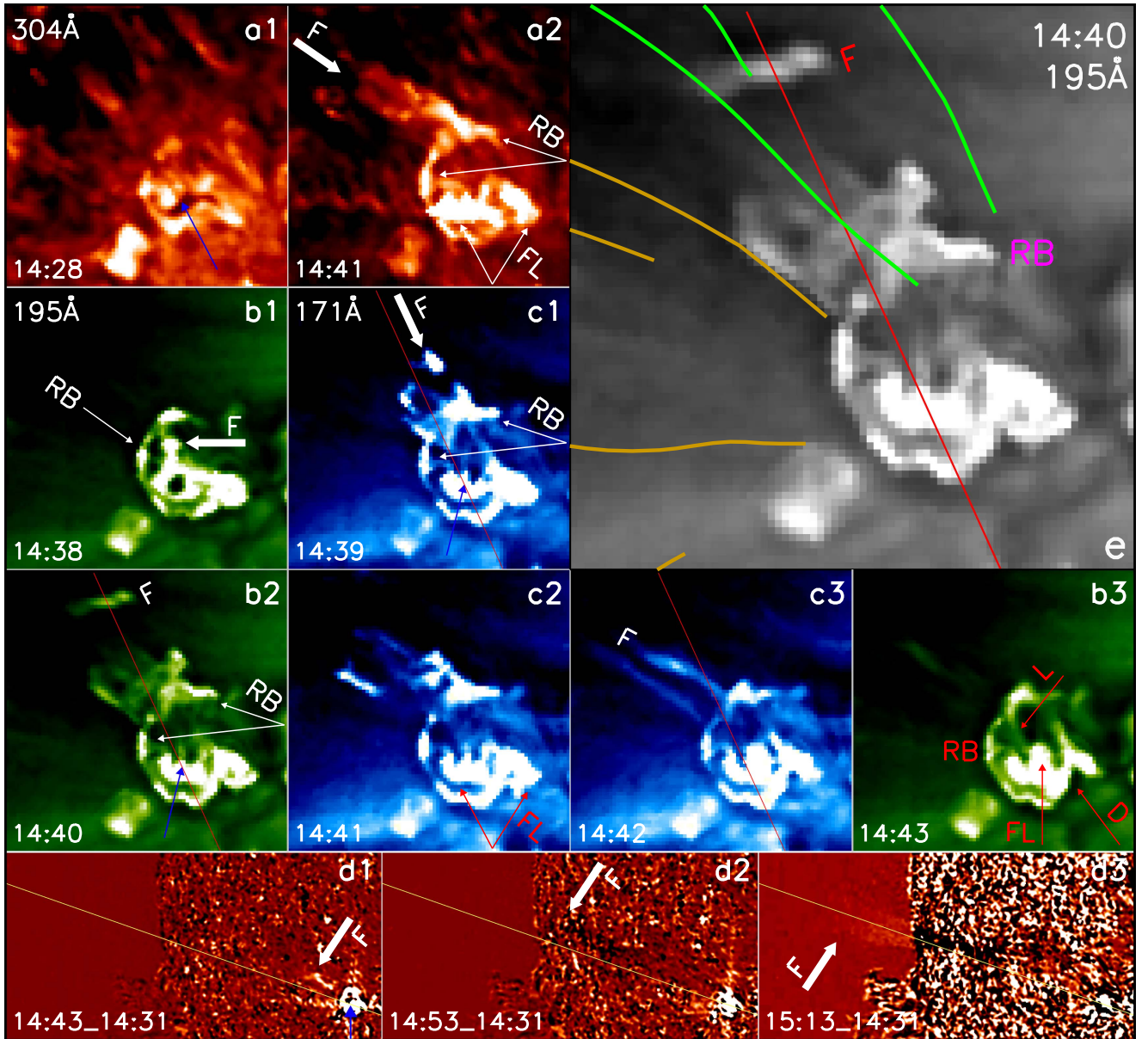


Figure 6. Filament eruption of 2010 November 15 in *STEREO-A/EUVI* 304 Å (a1)–(a2), 195 Å (b1)–(b3), and 171 Å (c1)–(c3) direct images with an FOV of $127'' \times 127''$, and in 304 Å fixed-base difference images (d1)–(d3) with an FOV of $762'' \times 381''$. Panel (e) is the *STEREO-A/EUVI* 195 Å direct image overlaid by the PFSS-extrapolated open- (green) and closed-field (brown) lines, with the same FOV as panels (a1)–(c3).

views. The streamer looked like a long southeast-oriented stalk-like feature with a diffuse bright base covering above the filament. The initial filament eruption direction, the ultimate filament eruption direction, and the final CME direction are marked by the red, yellow, and blue lines, respectively. The combined image of direct EUVI-A 195 Å and COR1- and COR2-A difference images at different times revealed that the CME was the production of the filament eruption, and its final direction was along the streamer (panel (b)). Moreover, the COR1-A observations provided key information of the deflection in the inner corona at the early CME stage (panels (d1)–(d6)). Clearly, the first CME signal was almost along the ultimate filament eruption direction shown by the yellow lines (panel (d1)). The CME gradually changed its propagation direction and then approach to its final trajectory (panels (d2)–(d4)). By about 15:45 UT, the CME front got to a projected height of $2.64 R_\odot$ over the solar surface, and then it

moved straight along the final direction (panels (a5)–(d6)). Likewise, the extrapolated PFSS coronal magnetic fields around the streamer base displayed a single-arcade bipolar configuration in the view of *STEREO-A* (panel (c)). Similar to the large deflection observed in the *SDO* view, the projected eruption direction underwent a counterclockwise rotation up to about 85° throughout the eruption process. Again, such a continuous direction deflection corresponded to the curved orientation of the green open-field lines. Thus it confirmed that the open field should be a crucial element in deflecting both the erupting filament and the early CME.

4. Magnetic Configuration Analysis

By combining with the PFSS-extrapolated results, it is found that the filament was located between the closed-field region and the open-field region around the northern flank of the

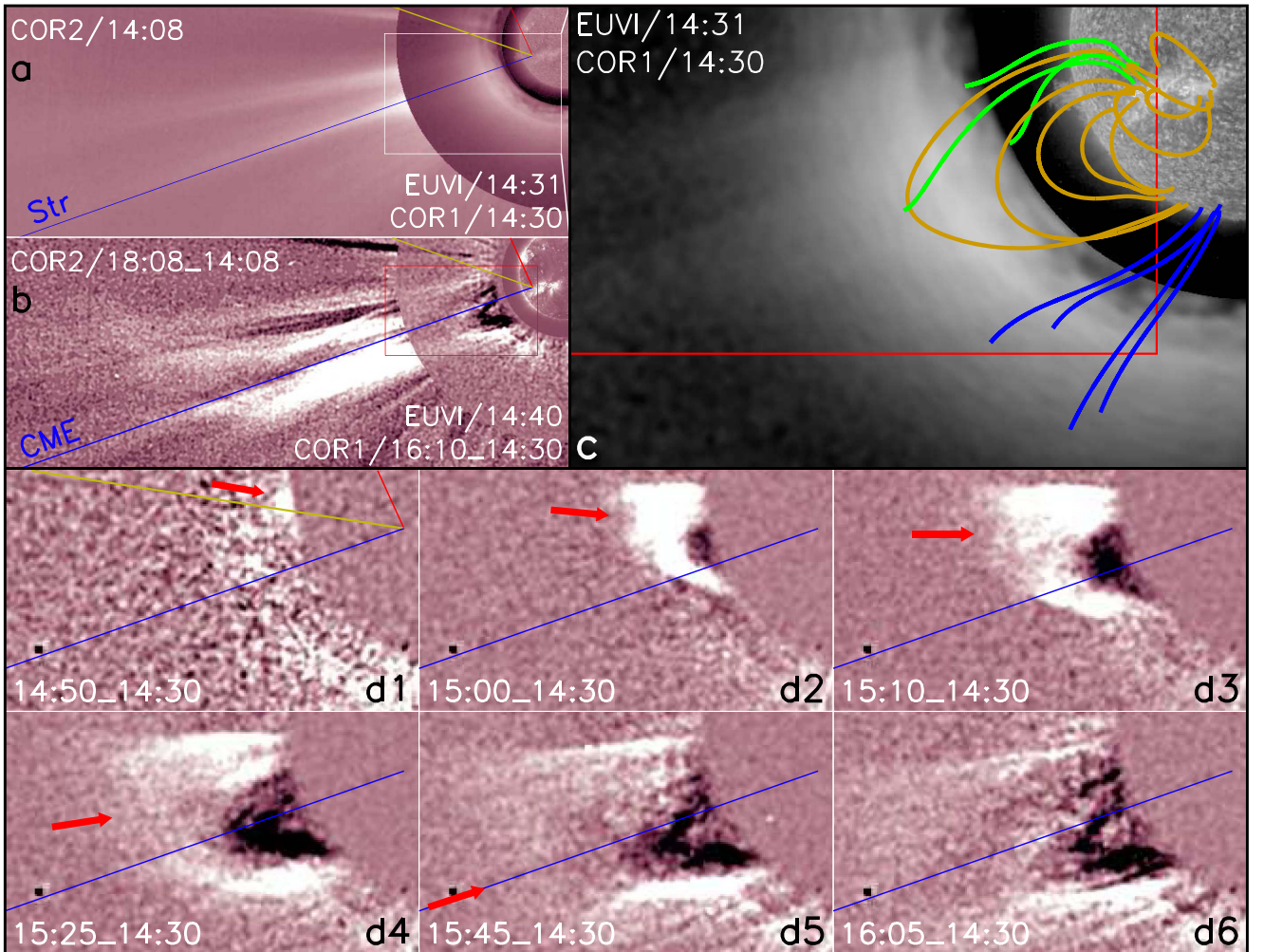


Figure 7. STEREO-A observations show the CME evolution on 2010 November 15. (a) The pre-existing streamer in composite image of direct EUVI 304 Å, COR1, and COR2 images. (b) Composite image of direct EUVI 195 Å, and fixed-base difference COR1 and COR2 images, showing the final projected CME direction. (c) Composite image of direct EUVI 304 Å and COR1 images overlaid by the PFSS-extrapolated open- (green and blue) and closed-field (brown) lines. (d1)–(d6) Fixed-base difference COR1 images, showing the CME deflection in the inner corona. The white box indicates the FOV for (c), and the red boxes indicate the FOV for (d1)–(d6). The thick red arrows point out the erupting CME.

streamer. The filament first erupted northwestward to the nearby open fields and produced clear interchange reconnection signals. Then the erupting filament was strongly deflected in latitude by the open-field lines that bent southward. The associated CME also showed a clear deflection and propagated along the streamer at final. These results strongly suggested that the erupting fields were first reconnected with and then guided by the northern open fields. Taking the magnetic field setting and connectivity around the eruptive region into account (see Figure 4(e)), the sketch displayed in Figure 8 illustrates our understanding of the event and can well explain most of the observed phenomena. The magnetic configuration around the filament before eruption is shown in panel (a). The plus signs mark the photospheric positive polarity, while the minus signs represent the negative polarity. The filament, F, denoted by the filled purple circles in the sketch, is initially held by an overlying arcade A (brown curves), which consists of closed fields of coronal loops; and the green curves indicate the open-field lines northwest to the filament. During the first eruption stage (panel (b)), the filament erupted northwestward and its overlying arcade expanded. The expanding external loops of

the arcade tended to and then met with the northwestern open fields. Thus the external reconnection occurred between them since the directions of their magnetic fields were nearly antiparallel at the contact point (shown by the red cross between the brown and the green curves). After the reconnection, the green open-field lines were closed to produce the remote brightenings, RB, and the loop system, L, and the brown closed loops were opened to form the coronal dimming region, D (panel (c)). Equivalently, such a course could be regarded as that the brown closed fields interchanged northwestward, and the green open fields jumped southeastward across the original filament F and its overlying arcade A. Therefore, this external reconnection was interchange reconnection, which changed the connectivity of the green open-field lines and the brown closed-field lines. Very similar to the scenarios described before (Sterling & Moore 2001; Crooker & Webb 2006; Yang et al. 2015), therefore, the occurrence of interchange reconnection was the cause of the simultaneous appearance of the remote brightenings, the dimming region, and the loop system in the initial eruption. At the same time, as the loops of the arcade stretched, their legs with different

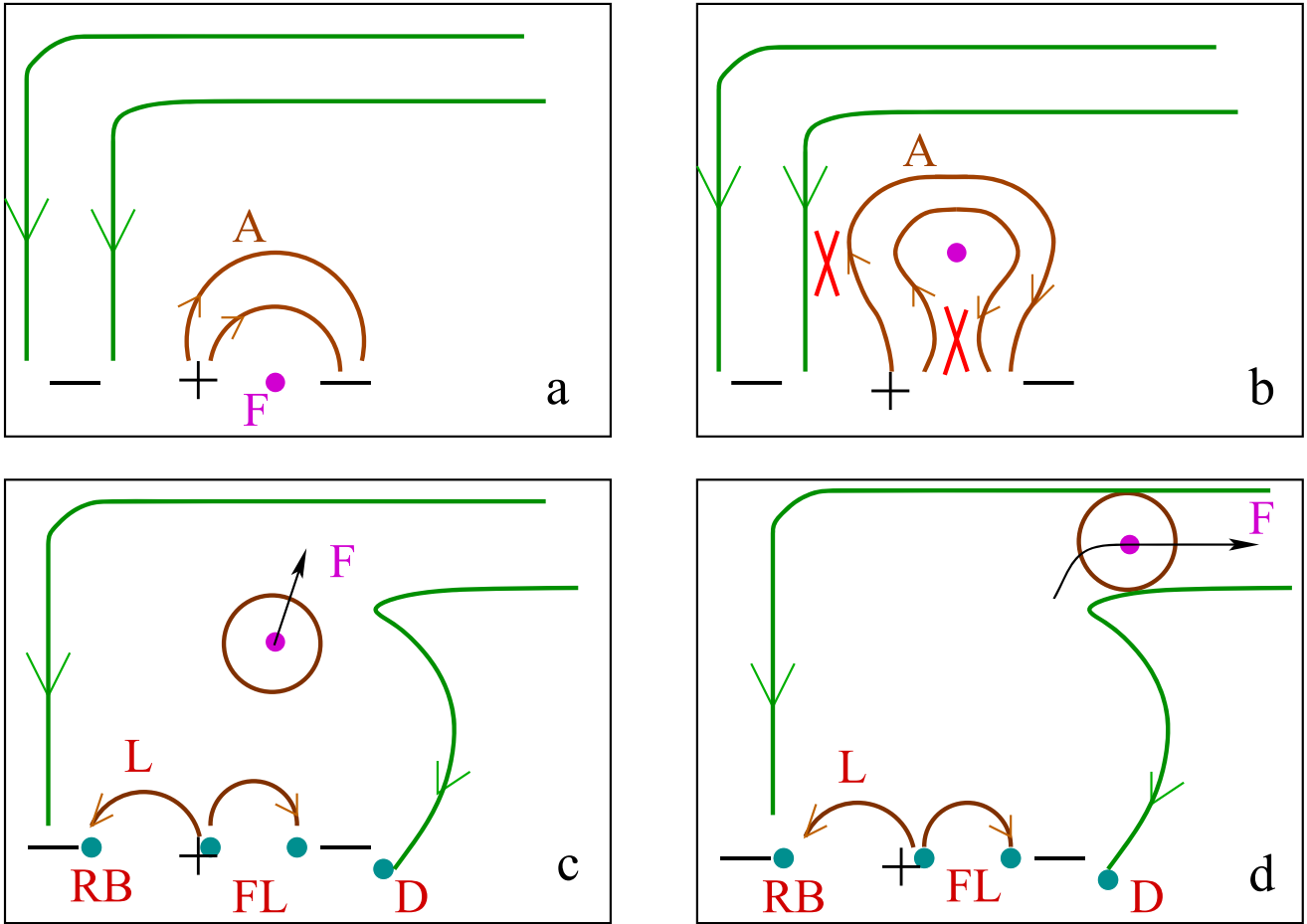


Figure 8. Sketch illustrating the eruption process of the filament on 2010 November 15 filament. The filament was first interacted with and then guided by the northern open fields. (a) Magnetic configuration before the filament eruption. The plus/minus signs mark the photospheric positive/negative polarities, while the open-/closed-field lines are plotted as the green/brown curves. (b) The raise of the filament led to the internal and the external reconnections. The red crosses label the sites of the internal/external reconnections. (c) The occurrence of the flare, FL, the remote brightenings, RB, the loop system, L, and the dimming region, D, as the outcomes of the internal and external reconnections. (d) The large-angle deflection of the erupting filament guided by the bent open-field lines.

magnetic polarities came closer and internal reconnection occurred in their interior (Sterling & Moore 2001; marked by the red cross near the brown curves). This internal reconnection produced the flare, FL, and a plasmoid, F (Moore & Sterling 2007), which is a toroidal coherent structure of filament's plasma and magnetic fields (panel (c)). Since the overlying arcade was opened by the interchange reconnection, the plasmoid exploded and escaped outward. However, it was guided by highly-bent open-field lines, resulting in the strong deflections of the filament and the CME (panel (d)). It is noted that the guiding effect of curved open-field lines was also suggested in some impulsive solar energetic particle events associated with EUV or white-light jets next to CHs (Wang et al. 2006). Similarly, Nisticò et al. (2015) investigated the trajectories of the polar coronal jets observed from 2007 March to 2008 April. They found that the propagation of the jets was not radial but deflected due to magnetic field lines, and the deflection of the jets over the north pole was larger than that of the jets over the south pole by order of 25%–40%.

5. Summary and Discussion

Using the data obtained by the *SDO*, the LASCO and the *STEREO-A*, we presented the eruption and the subsequent

large-angle deflection of a filament and the associated CME on 2010 November 15 from two different views. The main results are summarized as follows.

1. The filament was initially located between the closed-field region and the open-field region near the northern flank of a helmet streamer. This is a magnetic field configuration in favor of the occurrence of interchange reconnection.
2. The filament underwent a two-stage eruption. In *SDO* observations, there was a break of about 25 minutes between the two stages. However, *STEREO-A* observations showed that the two stages of the eruption were continuous, thus confirmed that they were from a single filament eruption.
3. The first stage of the filament eruption produced clear interchange reconnection signals, indicating the occurrence of interchange reconnection between the expanded overlying arcade and the ambient open fields. This event is one of the few examples that provided the direct observation signatures of interchange reconnection.
4. In the second stage, the eruption direction of the filament as well as the following CME deflected nearly 90° and approached to the radial direction of the streamer finally.

It is deduced that the deflection of the filament and the CME was due to the guide effect of the highly-bent open-field lines of the streamer. Such a large deflection of the filament eruption and the CME is remarkable, suggesting that we should pay enough attention to CME's near-Sun propagation in a space weather forecast.

The PFSS-modeled magnetic field configuration, the small size of the filament and its original location outside the base of the streamer arcade, and the initial eruption direction toward the northern open fields constituted the key elements of the event. The PFSS model clearly captured the large-scale streamer structure as seen in the coronagraph observations. The erupting filament first interacted with and then was guided by the north open field of the streamer, and the deflection of the trajectory resulted from the bending of the open-field lines. It appears that the computed northern open fields were not originated from a CH. Because ARs and magnetic plages are often the sources of open flux, it is common that such non-CH open fields and the associated streamer occur above an activity complex (Schrijver & DeRosa 2003; Zhao & Webb 2003; Liu 2007; Wang et al. 2007). Interestingly, the end height of the CME deflection at $2.64 R_{\odot}$ fell into the height range from 2 to $4 R_{\odot}$, within which the Y-type null point of a helmet streamer generally lied. This possibly suggests that the CME in present case was deflected toward the field strength minimum in the streamer configuration (Shen et al. 2011; Kay et al. 2013).

The initial filament eruption was away from the streamer arcade and approached the open fields, which was clearly different from the situations in some previous studies (Filippov & Gopalswamy 2001; Bemporad et al. 2005; Moore & Sterling 2007; Jiang et al. 2009; Panasenco et al. 2011). Hence the closed fields of the streamer should not play a part in eruption of the filament; and the sequent deflection should be caused by the channeling and guiding of the non-CH open fields. In agreement with the CH cases observed before (Jiang et al. 2007b; Gopalswamy et al. 2009; Kilpua et al. 2009), therefore, the erupting fields could not penetrate the magnetic wall of non-CH open fields although they interacted with each other at first. In this respect, the present event is very similar to the one on 2014 January 7, during which a fast CME was channeled by strong open fields surrounding its source region at the periphery of AR 11944 (Möstl et al. 2015; Wang et al. 2015). A cursory examination of AIA observations found that clear interchange reconnection signatures also appeared at the early stage of that event. A detailed study of the interaction between the erupting fields and the nearby open fields will be given in a separate paper.

We thank an anonymous referee for many constructive suggestions and thoughtful comments that improved the quality of this paper. The authors thank the *SDO*, *STEREO*, *SOHO*/LASCO teams, and the GONG/NSO consortium, for granting free access to their Internet databases. This work is supported by the National Natural Science Foundation of China under grants 11633008, 11333007, 11503081, and 11703084, by the CAS programs “Light of West China” and “QYZDJ-SSW-SLH012,” and by the grant associated with the Project of the Group for Innovation of Yunnan Province.

ORCID iDs

Jiayan Yang <https://orcid.org/0000-0003-3462-4340>

References

- Bemporad, A. 2009, *ApJ*, **701**, 298
 Bemporad, A., Sterling, A. C., Moore, R. L., & Poletto, G. 2005, *ApJL*, **635**, L189
 Bi, Y., Jiang, Y. C., Yang, J. Y., et al. 2013, *ApJ*, **773**, 162
 Bosman, E., Bothmer, V., Nisticò, G., et al. 2012, *SoPh*, **281**, 167
 Bothmer, V., & Mrotzek, N. 2017, *SoPh*, **292**, 157
 Brueckner, G. E., Howard, R. A., Koomen, M. J., et al. 1995, *SoPh*, **162**, 357
 Byrne, J. P., Maloney, S. A., McAteer, R. T. J., Rejojo, J. M., & Gallagher, P. T. 2010, *NatCo*, **1**, 74
 Cremades, H., & Bothmer, V. 2004, *A&A*, **422**, 307
 Cremades, H., Bothmer, V., & Tripathi, D. 2006, *AdSpR*, **38**, 461
 Crooker, N. U., Gosling, J. T., & Kahler, S. W. 2002, *JGRA*, **107**, 1028
 Crooker, N. U., & Webb, D. F. 2006, *JGR*, **111**, A08108
 Davies, J. A., Perry, C. H., Trines, R. M. G. M., et al. 2013, *ApJ*, **777**, 167
 Filippov, B. P., & Gopalswamy, N. 2001, *SoPh*, **203**, 119
 Gopalswamy, N., Mäkelä, P., Xie, H., Akiyama, S., & Yashiro, S. 2009, *JGRA*, **114**, A00A22
 Harrison, R. A. 1986, *A&A*, **162**, 283
 Howard, R. A., Moses, J. D., Vourlidas, A., et al. 2008, *SSRV*, **136**, 67
 Hundhausen, A. 1972, *Coronal Expansion and Solar Wind* (Berlin: Springer)
 Jiang, Y., Yang, J., Zheng, R., Bi, Y., & Yang, X. 2009, *ApJ*, **693**, 1851
 Jiang, Y., Yang, L., Li, K., & Ren, D. 2007a, *ApJL*, **662**, L131
 Jiang, Y., Yang, L., Li, K., & Shen, Y. 2007b, *ApJL*, **667**, L105
 Joshi, A. D., & Srivastava, N. 2011, *ApJ*, **730**, 104
 Kaiser, M. L., Kucera, T. A., Davila, J. M., et al. 2008, *SSRV*, **136**, 5
 Kay, C., Opher, M., & Evans, R. M. 2013, *ApJ*, **775**, 5
 Kilpua, E. K. J., Pomoell, J., Vourlidas, A., et al. 2009, *AnGeo*, **27**, 4491
 Kliem, B., Su, Y. N., van Ballegooijen, A. A., & DeLuca, E. E. 2013, *ApJ*, **779**, 129
 Lemen, J. R., Title, A. M., Akin, D. J., et al. 2012, *SoPh*, **275**, 17
 Li, T., Zhang, J., Zhao, H., & Yang, S. 2010, *ApJ*, **720**, 144
 Liu, Y. 2007, *ApJL*, **654**, L171
 Loughhead, R. E., Wang, J.-L., & Blows, G. 1983, *ApJ*, **274**, 883
 Lugaz, N., Downs, D., Shibata, K., et al. 2011, *ApJ*, **738**, 127
 Lugaz, N., Farrugia, C. J., Davies, J. A., et al. 2012, *ApJ*, **759**, 68
 Lynch, B. J., & Edmondson, J. K. 2013, *ApJ*, **764**, 87
 MacQueen, R. M., Hundhausen, A. J., & Conover, C. W. 1986, *JGR*, **91**, 31
 Mäkelä, P., Gopalswamy, N., Xie, H., Akiyama, S., & Yashiro, S. 2013, *SoPh*, **284**, 59
 Mays, M. L., Thompson, B. J., Jian, L. K., et al. 2015, *ApJ*, **812**, 145
 Moore, R. L., & Sterling, A. C. 2007, *ApJ*, **661**, 543
 Möstl, C., Rollett, T., Frahm, R. A., et al. 2015, *NatCo*, **6**, 7135
 Nisticò, G., Zimbardo, G., Patsourakos, S., Bothmer, V., & Nakariakov, V. M. 2015, *A&A*, **583**, A127
 Panasenco, O., Martin, S., Joshi, A. D., & Srivastava, N. 2011, *JASTP*, **73**, 1129
 Pesnell, W. D., Thompson, B. J., & Chamberlin, P. C. 2012, *SoPh*, **275**, 3
 Plunkett, S. P., Thompson, B. J., St., Cyr, O. C., & Howard, R. A. 2001, *JASTP*, **63**, 389
 Rodriguez, L., Zhukov, A. N., Cid, C., et al. 2009, *SpWea*, **7**, S06003
 Scherrer, P. H., Schou, J., Bush, R. I., et al. 2012, *SoPh*, **275**, 207
 Schrijver, C. J., & DeRosa, M. L. 2003, *SoPh*, **212**, 165
 Shen, C., Wang, Y., Gui, B., Ye, P., & Wang, S. 2011, *SoPh*, **269**, 389
 Shen, Y., Liu, Y., & Liu, R. 2011, *RAA*, **11**, 594
 Simnett, G. M. 2000, *JASTP*, **62**, 1479
 Sterling, A. C., Moore, R., & Harra, L. K. 2011, *ApJ*, **743**, 63
 Sterling, A. C., & Moore, R. L. 2001, *ApJ*, **560**, 1045
 Sun, X., Hoeksema, J. T., Liu, Y., Chen, Q., & Hayashi, K. 2012, *ApJ*, **757**, 149
 Wang, J., Li, W., Denker, C., et al. 2000, *ApJ*, **530**, 1071
 Wang, R., Liu, Y. D., Dai, X., et al. 2015, *ApJ*, **814**, 80
 Wang, Y., Shen, C., Wang, S., & Ye, P. 2004, *SoPh*, **222**, 329
 Wang, Y., Wang, B., Shen, C., Shen, F., & Lugaz, N. 2014, *JGRA*, **119**, 5117
 Wang, Y.-M., Pick, M., & Mason, G. M. 2006, *ApJ*, **639**, 495
 Wang, Y.-M., Sheeley, N. R., Jr., & Rich, N. B. 2007, *ApJ*, **658**, 1340
 Wuelser, J.-P., Lemen, J. R., Tarbell, T. D., et al. 2004, *Proc. SPIE*, **5171**, 111
 Xie, H., St., Cyr, O. C., Gopalswamy, N., et al. 2009, *SoPh*, **259**, 143
 Yan, X. L., Qu, Z. Q., Kong, D. F., Deng, L. H., & Xue, Z. K. 2013, *A&A*, **557**, A108
 Yang, J., Jiang, Y., Bi, Y., et al. 2012a, *ApJ*, **749**, 12

- Yang, J., Jiang, Y., Xu, Z., Bi, Y., & Hong, J. 2015, *ApJ*, **803**, 68
Yang, J., Jiang, Y., Yang, B., et al. 2012b, *SoPh*, **279**, 115
Yang, J., Jiang, Y., Zheng, R., et al. 2011, *SoPh*, **270**, 551
Yashiro, S., Michalek, G., Akiyama, S., Gopalswamy, N., & Howard, R. A. 2008, *ApJ*, **673**, 1174
Zhao, X. P., & Webb, D. F. 2003, *JGRA*, **108**, 1234
Zheng, R., Chen, Y., Du, G., & Li, C. 2016, *ApJL*, **819**, L18
Zheng, R., Chen, Y., Wang, B., Li, G., & Xiang, Y. 2017, *ApJ*, **840**, 3
Zhou, Y. F., & Feng, X. S. 2013, *JGRA*, **118**, 6007
Zuccarello, F. P., Bemporad, A., Jacobs, C., et al. 2012, *ApJ*, **744**, 66